

Cold season Africa–Asia multidecadal teleconnection pattern and its relation to the Atlantic multidecadal variability

Cheng Sun^{1,2} · Jianping Li^{1,2} · Ruiqiang Ding^{3,4} · Ze Jin⁵

Received: 18 January 2016 / Accepted: 5 August 2016 / Published online: 17 August 2016
© Springer-Verlag Berlin Heidelberg 2016

Abstract A prominent teleconnection pattern of multidecadal variability of cold season (November to April) upper-level atmospheric circulation over North Africa and Eurasia (NA–EA) is revealed by empirical orthogonal function analysis of the Twentieth Century Reanalysis data. This teleconnection pattern is characterized by an eastward propagating wave train with a zonal wavenumber of 5–6 between 20° and 40°N, extending from the northwest coast of Africa to East Asia, and thus is referred to as the Africa–Asia multidecadal teleconnection pattern (AAMT). One-point correlation maps show that the teleconnectivity of AAMT is strong and further demonstrate the existence of the AAMT. The AAMT shapes the spatial structure of multidecadal change in atmospheric circulation over the NA–EA region, and in particular the AAMT pattern and associated fields

show similar structures to the change occurring around the early 1960s. A strong in-phase relationship is observed between the AAMT and Atlantic multidecadal variability (AMV) and this connection is mainly due to Rossby wave dynamics. Barotropic modeling results suggest that the upper-level Rossby wave source generated by the AMV can excite the AAMT wave train, and Rossby wave ray tracing analysis further highlights the role of the Asian jet stream in guiding the wave train to East Asia. The AAMT acts as an atmospheric bridge conveying the influence of AMV onto the downstream multidecadal climate variability. The AMV is closely related to the coordinated change in surface and tropospheric air temperatures over Northwest Africa, the Arabian Peninsula and Central China, which may result from the adiabatic expansion/compression of air associated with the AAMT.

Electronic supplementary material The online version of this article (doi:10.1007/s00382-016-3309-y) contains supplementary material, which is available to authorized users.

✉ Jianping Li
ljp@bnu.edu.cn

¹ College of Global Change and Earth System Science (GCESS), Beijing Normal University, Beijing 100875, China

² Joint Center for Global Change Studies, Beijing 100875, China

³ State Key Laboratory of Numerical Modeling for Atmospheric Sciences and Geophysical Fluid Dynamics (LASG), Institute of Atmospheric Physics, Chinese Academy of Sciences, Beijing 100029, China

⁴ Plateau Atmosphere and Environment Key Laboratory of Sichuan Province, Chengdu University of Information Technology, Chengdu 610225, China

⁵ Department of Atmospheric Science, Yunnan University, Kunming 650091, China

Keywords Atlantic multidecadal variability · Africa–Asia multidecadal teleconnection pattern · Rossby wave train · Africa–Asia multidecadal climate variability

1 Introduction

Sea surface temperature (SST) variability over the North Atlantic basin has received considerable attention from the climate research community because it shows the largest potential for decadal predictability (Latif et al. 2006a; Corti et al. 2012). On decadal to multidecadal timescales, the North Atlantic SST variability is dominated by the Atlantic Multidecadal variability (AMV), which can be obtained as the leading empirical orthogonal function (EOF) mode of annual mean SST anomalies over the North Atlantic basin (Delworth et al. 2007). The AMV is characterized by a spatially coherent pattern with basin-wide warm/cold SST

anomalies. Thus, the AMV index can be easily defined as the area-weighted average of Atlantic SST anomalies north of the equator (Enfield et al. 2001; Sutton and Hodson 2005; Ting et al. 2009). In both reconstructions and observations the AMV shows an oscillatory behavior between warm and cold phases with a period of 50–70 years (Schlesinger and Ramankutty 1994; Gray 2004). Several mechanisms have been proposed to explain the AMV, such as ocean heat transport associated with variations in the Atlantic meridional overturning circulation (AMOC; Delworth and Mann 2000; Vellinga and Wu 2004; Knight et al. 2005; Gastineau and Frankignoul 2011), fluctuations in the external climate forcing (e.g., solar radiation and atmospheric concentrations of anthropogenic and natural aerosols; Booth et al. 2012), and changes in wind stress forcing and decadal scale air-sea coupling (Latif et al. 2006b; Latif and Keenlyside 2011). In particular, recent studies have suggested that the AMV is linked to the decadal fluctuations of the North Atlantic Oscillation (NAO), a dominant mode of atmospheric circulation variability in the North Atlantic (Greatbatch 2000). There is a two-way interaction between the NAO and AMV, with the NAO leading the AMV by 15–20 years while the AMV provides a delayed negative feedback to the NAO, and this interaction may lead to the quasi-periodic multidecadal cycle of the AMV (Li et al. 2013; Sun et al. 2015a).

The persistent basin-scale SST anomalies associated with the AMV have significant effects on the climate of the surrounding land masses. The AMV has been linked to rainfall variability in the United States (Enfield et al. 2001; Nigam et al. 2011), and during the warm (cold) AMV phase, most of the United States receives less (more) than normal rainfall. The warm (cold) phase of the AMV can weaken (strengthen) the North Atlantic subtropical high and result in decreased (increased) moisture flow into the United States. Meanwhile, positive correlations have been found between the AMV index and rainfall amounts in northwest Europe and the Sahel (Sutton and Hodson 2005; Zhang and Delworth 2006). With respect to land surface air temperature (LSAT) variations, previous studies have linked a warm AMV phase to warmer-than-normal LSAT over North America and western Europe (Sutton and Hodson 2005, 2007; Ting et al. 2009). Hurricane activity over the North Atlantic basin has also been related to the AMV (Zhang and Delworth 2006). This is due not only to the SST anomalies but also to changes in vertical shear in the troposphere over the main hurricane development region. In addition, the AMV has been connected to multidecadal variations in the polar atmospheric circulation due to the large amplitude of the SST anomaly in the subpolar North Atlantic, and the warm (cold) AMV phase is associated with weakening (strengthening) of the stratospheric polar vortex in winter (Omrani et al. 2015).

The AMV can exert remote influences on climate variability outside the North Atlantic region. Both observations and numerical simulations have suggested that the AMV has a direct warming/cooling effect on the surface temperature averaged over the entire Northern Hemisphere (NH) and that the multidecadal variability in NH mean surface temperature can be largely explained by the AMV (Knight et al. 2005; Zhang et al. 2007; Li et al. 2013). The AMV has a remote impact on the Siberian warm season rainfall through a Rossby wave train across the northern Eurasian continent (Sun et al. 2015b), and the AMV also influences decadal variability of heat wave frequency over Eurasia (Zhou and Wu 2016). During summer, a positive correlation has been found between the strength of the Indian summer monsoon and the AMV (Zhang and Delworth, 2006; Li et al. 2008). Several mechanisms have been put forward to explain this teleconnection, including the meridional shift of the Intertropical Convergence Zone and a Rossby-wave response in the troposphere induced by the Atlantic SST anomalies (Kucharski et al. 2006, 2009). Meanwhile, the East Asian summer monsoon is also likely to be stronger during the warm AMV phase (Lu et al. 2006). During winter, the AMV also shows some connection with East Asian climate. There is some observational and modeling evidence that the warm AMV phase is associated with a weaker East Asian winter monsoon (EAWM) and warmer-than-normal LSAT over most of China (Li and Bates 2007; Wang et al. 2009; Ding et al. 2014). Nevertheless, the dynamical mechanism underlying this wintertime teleconnection is still unclear and the pathway linking the AMV to EAWM multidecadal variability remains to be elucidated.

The Asian jet stream in the upper troposphere plays an important role in the downstream propagation of perturbations from the North Atlantic region. Previous theoretical studies have demonstrated that the subtropical jet stream acts as a Rossby waveguide along which Rossby waves can propagate and tend to be trapped (Hoskins and Ambrizzi 1993). Observational studies have provided further evidence for the waveguide effect of the jet stream. During summer, the variability of NH mid-latitude atmospheric circulation is dominated by a circumglobal teleconnection (CGT) pattern (Ding and Wang 2005), which is characterized by a Rossby wave train along the subtropical jet stream and is closely associated with South Asian monsoon variability. The CGT over the Eurasian continent has also been referred to as the Silk Road pattern (Lu et al. 2002; Enomoto et al. 2003), and the Eurasian wave train is linked to interannual variability of regional climate and monsoon circulation (Wu et al. 2012, 2015). The winter jet stream is stronger than its summer counterpart. Previous studies have identified a winter circumglobal waveguide pattern in the NH extratropical atmospheric circulation, exhibiting a

strong zonal wavenumber 5 component with peak amplitude around the latitude of the Asian jet stream (Hsu and Lin 1992; Branstator 2002). Meanwhile, along the Asian jet waveguide, the winter NAO can exert a strong downstream influence on the East Asian climate by exciting a zonally oriented wave train pattern that extends from the Mediterranean Sea toward East Asia and the North Pacific (Watanabe 2004). However, most studies addressing the teleconnection pattern along the Asian jet stream have focused on intraseasonal to interannual timescales (Hsu and Lin 1992; Lu et al. 2002; Branstator 2002; Enomoto et al. 2003; Ding and Wang 2005; Watanabe 2004), while at multidecadal timescales the existence of such teleconnection patterns has not been well understood. Moreover, it remains unclear whether the AMV can excite a Rossby wave train in the cold season and whether the Asian jet waveguide plays a role. This is not only important for understanding the multidecadal variability of atmospheric circulation, but also extends our knowledge of the climate impacts of the AMV. The remainder of the paper is structured as follows. The datasets and methodology used in the analysis are described in Sect. 2. Section 3 presents the results of this study and is divided into three parts in order to address the above issues. Finally, a discussion and summary of the results are provided in Sect. 4.

2 Data and methodology

2.1 Data

Several datasets are employed in the present analysis. Atmospheric data including wind fields, air temperature and geopotential height are obtained from the Twentieth Century Reanalysis Version 2 (20CRv2) which is generated by assimilating global surface pressure observations and prescribing SST and sea ice distributions as boundary conditions for the atmosphere (Compo et al. 2011). The 20CRv2 dataset covers the period 1871–2012 with $2^\circ \times 2^\circ$ spatial resolution and has been widely used in studies of multidecadal climate variations. SST data are taken from the NOAA Extended Reconstruction SST version 3 (ERSST v3b) dataset (Smith et al. 2008), with 2° latitude by 2° longitude resolution covering the period 1854–2012. Observational global SST data derived from the Hadley Centre SST dataset (HadISST; Rayner et al. 2003) are also employed to test the reliability of the results. Results from the two SST datasets are similar, and thus we show only the results from the ERSST data. Two sets of monthly LSAT data are used: (1) LSAT data from the Climate Research Unit (CRU) high-resolution surface climate dataset CRU TS 3.23 (Harris et al. 2014), covering the period 1901–2012

on a $0.5^\circ \times 0.5^\circ$ grid, and (2) LSAT data developed by the Goddard Institute for Space Studies (GISS; Hansen et al. 2010), available on a $2^\circ \times 2^\circ$ grid for the period 1880–2012. To compare the results between the two datasets and to focus on relatively large-scale variability, the CRU LSAT data were re-gridded onto a coarser resolution (around 2° latitude/longitude) using the distance-weighted averaging interpolation method. As the results are not sensitive to either choice, here we show only the results based on the CRU LSAT data unless specified otherwise.

Because uncertainties in surface observations prior to 1900 are relatively large and the data before 1900 are deemed less reliable (Folland et al. 2001; DelSole et al. 2011), we confine our analysis to the post-1900 period for all the data. Prior to the analysis, all the variables are linearly detrended over the analysis period using the least squares method. Our intent is to remove the centennial scale trends to better isolate and highlight the signal of decadal to multidecadal variability. We focus on the NH cold season (November to April) when the Asian jet stream is strong, and cold season means are constructed for SST, LSAT, and atmospheric data (e.g., winds, geopotential height) by averaging values from November to April. The upper-level meridional wind at 300 hPa (V300) is of special interest here because it has almost no zonal mean and is very useful in representing the dynamics of mid-latitude planetary waves and teleconnections (Branstator 2002; Teng and Branstator 2012).

2.2 Statistical methods

To identify the dominant multidecadal teleconnection pattern along the Asian jet stream, we perform EOF analysis on the cold season V300 across the Eurasian continent ($0\text{--}60^\circ\text{N}$, $30^\circ\text{W}\text{--}150^\circ\text{E}$). Before applying the EOF, the V300 anomalies are smoothed with an 11-year running mean filter to isolate the multidecadal signal, and area weighting is accomplished by multiplying the V300 field by the square root of the cosine of latitude (Sun et al., 2013). The statistical significance of the linear regression coefficients and the correlation between two auto-correlated time series is ascertained via a two-tailed Student's t test using the effective number of degrees of freedom (Li et al. 2013). The effective number of degrees of freedom N^{eff} can be given by the following approximation:

$$\frac{1}{N^{\text{eff}}} \approx \frac{1}{N} + \frac{2}{N} \sum_{j=1}^N \frac{N-j}{N} \rho_{XX}(j) \rho_{YY}(j), \quad (1)$$

where N is the sample size, and $\rho_{XX}(j)$ and $\rho_{YY}(j)$ are the autocorrelations of two sampled time series X and Y , respectively, at time lag j .

2.3 Tools for analyzing Rossby wave propagation

Wave activity analysis was applied to investigate the stationary Rossby wave energy propagation. The wave activity flux is parallel to the group velocity of stationary Rossby waves, and thus is a useful indicator for identifying the propagation direction and source of stationary Rossby waves in the atmosphere. The wave activity flux is calculated following the method described in Plumb (1985).

Rossby wave ray tracing theory further allows us to trace the trajectory of the stationary Rossby wave train and characterize the impact of basic flow on the propagation behavior of wave energy. The theory was developed by Hoskins and Karoly (1981) and Hoskins and Ambrizzi (1993). The trajectory of the wave ray can be calculated numerically based on the angle of the wave front propagation, which is determined by the ratio between zonal and meridional group velocities. In this study, the stationary Rossby wave ray was calculated following the methodology described in Li et al. (2015).

2.4 Linear barotropic model

The linear barotropic model is a steady model with a horizontal resolution of T42 and consists of a simple barotropic vorticity equation given as:

$$J(\bar{\psi}, \nabla^2 \psi') + J(\psi', \nabla^2 \bar{\psi} + f) + \nu \nabla^6 \psi' + \alpha \nabla^2 \psi' = S', \quad (2)$$

where J represents a Jacobian operator, $\bar{\psi}$ and ψ' are basic state and perturbation streamfunctions, respectively, f is the Coriolis parameter, and S' is the anomalous vorticity source induced by the divergence. The biharmonic diffusion coefficient ν is chosen to be $2 \times 10^{16} \text{ m}^4 \text{ s}^{-1}$ in order to dampen small-scale eddies in 1 day, while the Rayleigh friction coefficient α is set to $(10 \text{ days})^{-1}$ (Sun et al. 2014, 2015b).

3 Results

3.1 Identification of Africa–Asia multidecadal teleconnection pattern

We begin with the analysis of the dominant mode of decadal variability in the V300. Figure 1 shows the first leading EOF mode (EOF1) for the 11-year running mean V300 anomalies across the Eurasian continent ($0\text{--}60^\circ\text{N}$, $30^\circ\text{W}\text{--}150^\circ\text{E}$). The EOF1 of the decadal V300 captures 30 % of the filtered variance, and is statistically distinguished from the second EOF (12 % of the variance) according to the criterion given by North et al. (1982). The EOF1 pattern (Fig. 1a) is characterized by a zonal wave structure with alternate centers of southerly and northerly

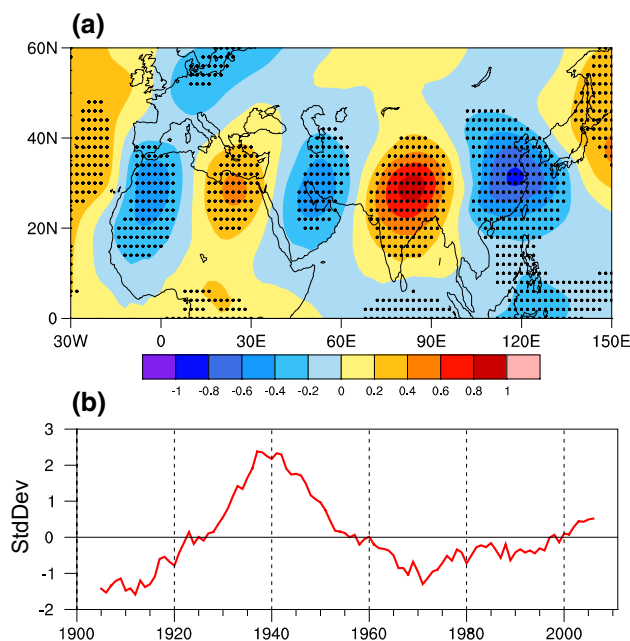


Fig. 1 **a** The spatial pattern and **b** corresponding normalized PC time series of the first EOF mode for the 11-year running mean cold season V300 anomaly over the Eurasian continent ($0\text{--}60^\circ\text{N}$, $30^\circ\text{W}\text{--}150^\circ\text{E}$). The EOF pattern is displayed as V300 anomaly (m s^{-1}) regressions onto the corresponding normalized PC. *Dots* in **a** indicate the regressions significant at the 95 % confidence level, and in the *dotted* areas, the N^{eff} varies spatially between 5 and 15

anomalies extending from the northwest coast of Africa to East Asia. Over North Africa and Eurasia (NA–EA), the EOF1 pattern shows two positive and three negative centers of action of V300 anomalies located along the latitudes between 20°N and 40°N , corresponding to a zonal wave-number of approximately 5–6. The principal component (PC) time series of EOF1 (Fig. 1b) exhibits clear multidecadal variations over the past century. In particular, the EOF1 was in a negative phase prior to the 1920s and during the 1960s to 1990s while in a positive phase for the period 1930–1960 and after 2000. Because the EOF1 extends from Northwest Africa to East Asia and shows multidecadal fluctuations, the EOF1 is referred to hereinafter as the Africa–Asia multidecadal teleconnection pattern (AAMT) and the associated PC time series as the AAMT index. We also examine the EOFs for the decadal meridional wind anomaly at 200 and 400 hPa, and the AAMT can also be obtained as the EOF1 of these anomalies. This indicates that the definition of AAMT is insensitive to the choice of a specific vertical level in the mid and upper troposphere.

In order to test how sensitive the AAMT is to the data filtering, we performed a similar EOF analysis but to the unfiltered V300 field. Figure S1 of the Supplementary Material shows the four leading EOFs of cold season NA–EA V300 anomalies and the associated PCs from the

20CRv2 dataset. These four leading EOFs explain 20, 17, 14 and 10 % of the total variance, respectively, and they explain 61 % of the total variance together. Although the four EOF patterns all show zonal wave structures, only the fourth leading EOF mode (EOF4) strongly projects on the AAMT pattern. The EOF4 is characterized by five centers of action of V300 anomalies along the 30°N latitude circle, consistent with the spatial features of AAMT. We also analyzed the temporal features of the four PC time series. Power spectral analysis was applied to detect the predominant timescales of the four EOF modes (Fig. S2 of the Supplementary Material). The spectra of the first three EOF modes show enhanced variance at interannual–decadal timescales (<30 year) but much reduced variance at multidecadal timescales (>30 year). In contrast, the spectrum of EOF4 is characterized by a high and significant concentration of variance at multidecadal timescales but much less variance at interannual timescales. This indicates that the EOF4 has a preference for variability in the multidecadal range. The smoothed PC time series of EOF4 is also highly correlated with the AAMT index ($r = 0.92$). Therefore, these results suggest that the EOF4 of unfiltered V300 anomalies corresponds to the AAMT and that the existence of AAMT is independent on the data filtering. Moreover, the AAMT can also be obtained as the EOF1 of the 5-year running mean V300 anomalies (not shown here), further indicating that the AAMT is robust to the choice of the running window length.

In this study, the cold season is defined as the 6 months between November to April, and it is necessary to check how the AAMT changes with seasonal March. The AAMT is obtained as the EOF1 of the decadal V300 across the Eurasian continent. We repeated the EOF analysis, but the analysis was done separately for the two 3-month seasons November–January (NDJ) and February–April (FMA). Figure S3 of the Supplementary Material shows the EOF1 modes of the decadal NA–EA V300 anomalies for NDJ and FMA seasons and the corresponding PC time series. The EOF1 modes of NDJ and FMA V300 anomalies both show a zonal wave train pattern with five centers of action extending from the northwest coast of Africa to East Asia, and the associated wave propagation is primarily confined between 20°N and 40°N. These two EOF1 patterns both strongly project on the AAMT, indicating that the structure of AAMT pattern is generally maintained from NDJ to FMA. Although the main spatial features (i.e., the approximate locations of the centers of action) of the NDJ and FMA EOF1 patterns are similar, it should be noted that the magnitudes of the FMA EOF1 patterns are slightly weaker than the NDJ counterpart, particularly for the downstream portion of the wave train. The PC time series of the NDJ and FMA EOF1 modes are highly correlated ($r = 0.83$, significant at the 95 % confidence level), and the correlations

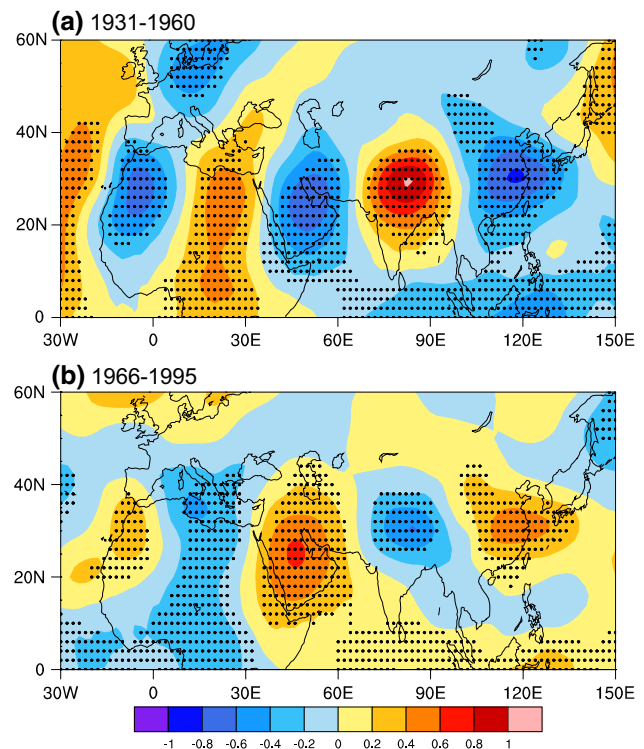
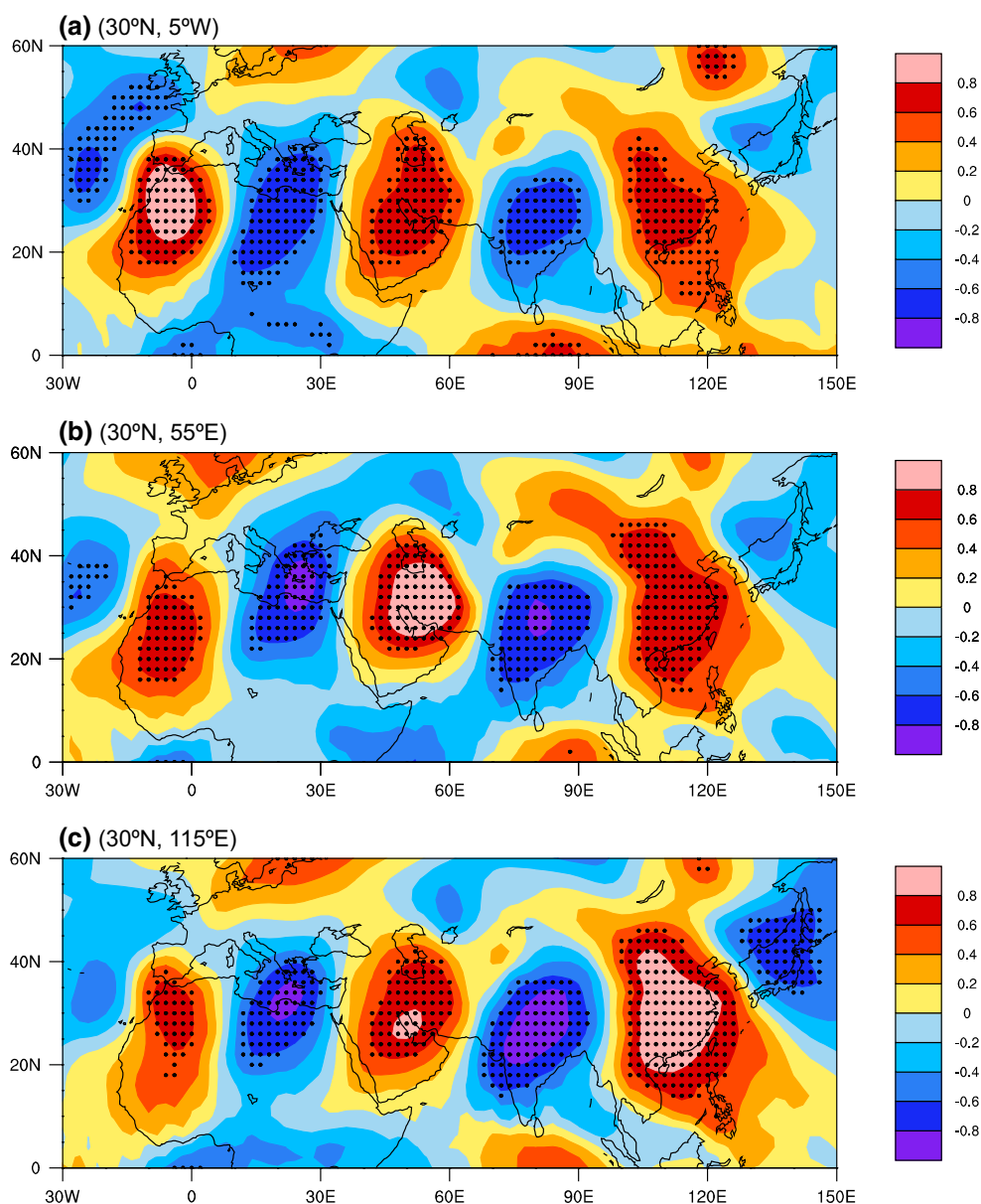


Fig. 2 30-year averages of cold season V300 anomalies for **a** 1931–1960 and **b** 1966–1995. The anomalies are computed relative to the 1900–2010 climatology. *Dots* in **a** and **b** indicate the regions where the 30-year averaged V300 is significantly different from the climatology at the 95 % confidence level (student's *t* test)

of the two PC time series with the AAMT index are 0.80 and 0.81, respectively, both significant at the 95 % confidence level. Therefore, the spatial–temporal features of the EOF1 modes for the decadal NDJ and FMA V300 are generally consistent with the AAMT derived from the cold season mean data.

The AAMT index shows that a phase transition from positive to negative phase occurred in the early 1960s. In order to investigate whether the observed atmospheric circulation experienced a similar change, we compare the AAMT pattern with the multidecadal change in upper-level atmospheric circulation. Figure 2 shows the multidecadal averages of V300 anomalies for two consecutive 30-year periods (1931–1960 and 1966–1995). The pattern of V300 anomalies averaged over 1931–1960 exhibits a zonal wave train structure, consisting of three negative centers over Northwest Africa, the Arabian Peninsula and East Asia, and two positive centers over Northeast Africa and North India. The V300 anomalies for 1966–1995 show a similar zonal teleconnection pattern to the preceding 30-year period, but with the sign of the anomalies reversed. This indicates that the multidecadal atmospheric circulation pattern in the upper troposphere indeed experienced a remarkable change around the early 1960s. Moreover, the spatial patterns of

Fig. 3 One-point correlation maps between cold season V300 at base points **a** (30°N, 5°W), **b** (30°N, 55°E) and **c** (30°N, 115°E) and V300 over the Eurasian continent. The correlations are calculated based on 11-year running mean data. *Dots* in **a–c** indicate the correlations significant at the 95 % confidence level, and in the *dotted* areas, the N^{eff} varies spatially between 8 and 15, 7 and 15 and 8 and 16, respectively



the multidecadal variations in the V300 closely resemble the AAMT, further suggesting that the AAMT makes an important contribution to the V300 multidecadal variability.

As shown in Fig. 1a, the AAMT has three negative (5°W, 55°E and 115°E) and two positive (25°E and 85°E) centers of action along the 30°N latitude circle. To examine the temporal coherence between the centers of action in the AAMT pattern or the teleconnectivity of AAMT, we calculated the one-point correlations maps of decadal V300 anomalies with reference to each of the five centers of action. Figure 3 shows the results only for the three negative centers, because the results for the two positive centers are similar but with the sign reversed. The three one-point correlation maps all exhibit the AAMT characteristics and show high and significant correlations (significant at the

95 % confidence level) over all the centers of action, suggesting that the five centers of action share a large part of their respective decadal variability and that the teleconnectivity of the AAMT pattern is strong.

To investigate the vertical structure of the AAMT pattern, we calculated the latitudinal averages of meridional wind and geopotential height at 20°–40°N regressed onto the AAMT index over decadal timescales (Fig. 4a). The meridional wind anomalies associated with the AAMT show strongly equivalent barotropic structure in the troposphere with maxima located in the upper troposphere. The geopotential height field shows three centers of maximum positive anomalies in the upper troposphere extending from the northwest coast of Africa to East Asia with minimum anomalies in between. These positive height

Fig. 4 **a** Cold season meridional wind (contours, m s^{-1}) and geopotential height anomalies (shading, m) regressed onto the normalized AAMT index at decadal timescales. *Dots* indicate the regressions for height significant at the 95 % confidence level, and in the *dotted* areas, the N^{eff} varies spatially between 6 and 15. **b** Multidecadal differences in meridional wind (contours, m s^{-1}) and geopotential height (shading, m) between two 30-year periods 1931–1960 and 1966–1995. *Dots* indicate the regions where the 30-year averaged heights for the two periods are significantly different at the 95 % confidence level (student's *t* test)

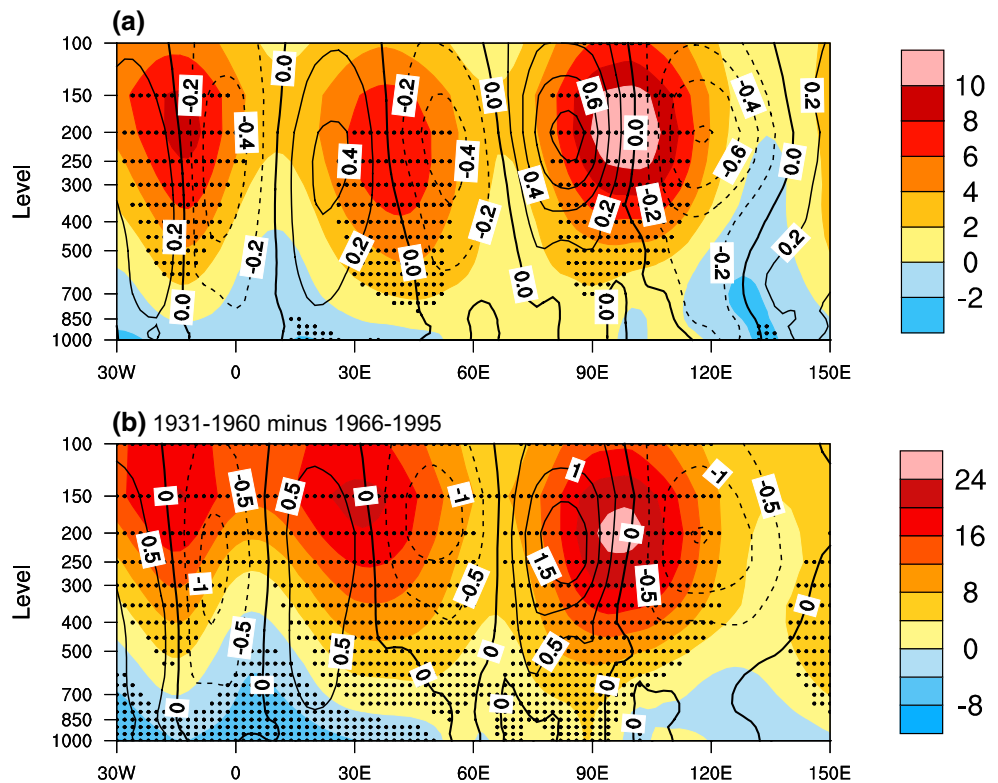
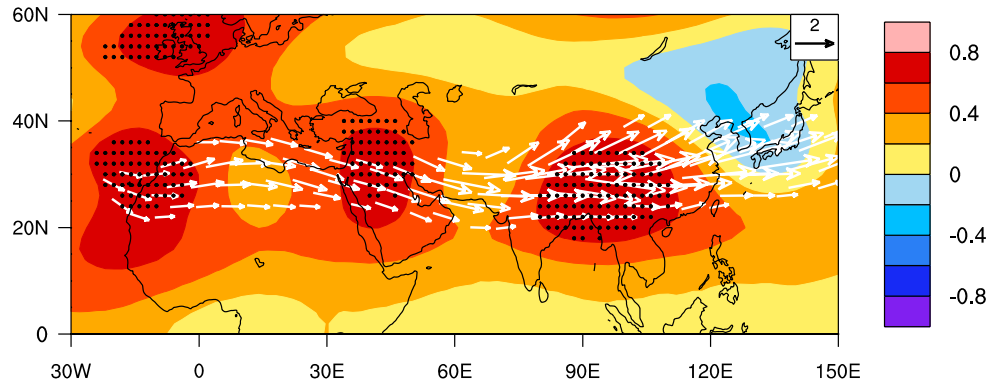


Fig. 5 Correlations of cold season 300-hPa geopotential height with the AAMT index at decadal timescales. *Dots* indicate correlations significant at the 95 % confidence level, and in the *dotted* areas, the N^{eff} varies spatially between 6 and 14. *Vectors* ($\text{m}^2 \text{s}^{-2}$, omitted below $1 \text{ m}^2 \text{s}^{-2}$) denote horizontal stationary wave activity flux associated with the wave train pattern



anomalies tend to intensify the climatological ridge over Europe but weaken the East Asian trough. The locations of the maxima and minima of the regressed geopotential height anomalies correspond to the zero-value contours of the meridional wind anomalies and are consistent with the geostrophic wind relationship. The AAMT vertical structure is also compared to the multidecadal change in the latitudinally averaged atmospheric circulation. As shown in Fig. 4b, the multidecadal meridional wind and geopotential height during 1966–1995 are significantly different from the preceding 30-year period (1931–1960) throughout the troposphere. Moreover, the multidecadal change patterns of meridional wind and geopotential height are highly consistent with the vertical structure of the AAMT pattern, further indicating that the AAMT makes a large contribution to the

multidecadal change in the NA–EA tropospheric atmospheric circulation occurring around the early 1960s.

To explore the dynamic mechanism of the AAMT pattern, we analyzed the horizontal component of the wave activity flux. Figure 5 depicts the horizontal wave activity flux associated with the AAMT together with the geopotential height field. The correlation map between the decadal geopotential height and AAMT index exhibits a zonal wave train pattern with three high positive correlation centers over Northwest Africa, the Arabian Peninsula and East Asia and two weak insignificant correlation centers in between. Meanwhile, the wave activity flux in the upper troposphere is mainly zonal in direction and eastward propagation of stationary wave energy is obviously seen over the NA–EA region. The wave activity flux is confined mainly between

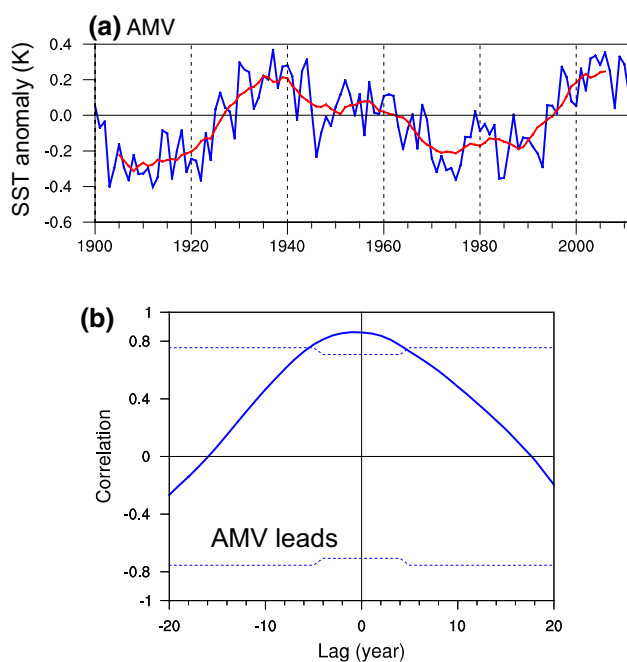


Fig. 6 **a** Cold season AMV index (blue, K) and the 11-year running mean (red) for the period 1900–2012. **b** Lead–lag correlation between the AAMT and AMV indices at decadal timescales. Negative (positive) lags indicate that the AMV is leading (lagging) and the blue dashed lines are the 95 % confidence levels based on the effective numbers of degrees of freedom (N^{eff}), and the N^{eff} varies between 6 and 7 from lag -20 to 20 years

20°N and 40°N , originating from the northwest coast of Africa and propagating toward East Asia. This propagation feature is suggestive of the Rossby wave dynamics leading to the upper tropospheric atmospheric circulation patterns associated with the AAMT.

3.2 Dynamical linkage between AAMT and AMV

The wave activity flux associated with the AAMT originates from the regions adjacent to the North Atlantic. The AMV is the dominant mode of North Atlantic SST variability, characterized by the multidecadal oscillation of SST between warm and cold anomalies over the entire basin. Thus, we hypothesize that the multidecadal SST change associated with the AMV may play a key role in forcing the wave train pattern of the AAMT. This hypothesis is supported by the correlation analysis between the AAMT and AMV indices. The AMV index (Fig. 6a) is defined as the area-averaged North Atlantic SST anomalies ($7.5\text{--}75^{\circ}\text{W}$, $0\text{--}60^{\circ}\text{N}$) for the cold season, which shows negative phases before the 1920s and during the 1960s to 1990s and positive phases during the 1920s to 1960s and after the late 1990s. The multidecadal fluctuations in the AMV index appear to be approximately in phase with those in the AAMT index (Fig. 1). Figure 6b further shows the lead–lag

correlation of the smoothed AMV index (11-year running mean) with the AAMT index. A high correlation coefficient ($r = 0.84$, significant at the 95 % confidence level) is observed between the AMV and AAMT at zero lag. This indicates that the multidecadal variations in the AAMT can be largely explained by the AMV.

The spatial patterns of the AMV–AAMT relationship are further analyzed. Figure 7a depicts the correlation map between the AAMT index and cold season North Atlantic SST anomalies, showing a basin-wide uniform pattern with significant positive values that resembles the AMV. On the other hand, the correlation map of the cold season V300 anomalies with the AMV index (Fig. 7b) exhibits a zonal wave train pattern with alternate centers of significant positive and negative correlations between 20°N and 40°N , in good agreement with the wave structure of AAMT. Furthermore, we apply maximum covariance analysis (MCA; Bretherton et al. 1992) to the cross-covariance matrix between cold season North Atlantic SST and Eurasian V300 anomalies ($0\text{--}60^{\circ}\text{N}$, $30^{\circ}\text{W}\text{--}150^{\circ}\text{E}$) over decadal timescales. The leading MCA mode explains 80 % of the total squared covariance. The time series of the expansion coefficients associated with this mode are strongly correlated ($r = 0.90$, significant at the 95 % confidence level). The expansion coefficients of the SST and V300 fields show strong correlations of 0.95 and 0.94 with the smoothed AMV and AAMT indices, respectively. Figure 7c, d display the leading pair of heterogeneous patterns generated by correlating the respective heterogeneous field with the MCA leading normalized expansion coefficients. The pattern for SST bears a strong resemblance to the AMV, with significant positive correlations over the whole North Atlantic, while the pattern for V300 strongly projects onto the AAMT. Thus, these results further suggest that the AMV–AAMT relationship is strong and robust.

Basin-scale SST anomalies can result in large-scale convergence/divergence anomalies in the upper troposphere, which may act as a source of stationary Rossby wave activity (Hodson et al. 2010; Sun et al. 2015b). In order to understand the dynamic mechanism for the AMV–AAMT linkage, we examine the cold season upper-level divergence and Rossby wave source (RWS) associated with the AMV (Fig. 8a). The velocity potential and divergent winds suggest that anomalous upper-level divergence occurs over the North Atlantic during the warm AMV phase. This is consistent with previous findings that upper-level divergent outflow prevails during the warm AMV phase due to the diabatic heating and ascending motion in response to the North Atlantic warming (Hodson et al. 2010; Alexander et al. 2014). The anomalous wind divergence may produce a strong RWS anomaly (Watanabe 2004). As seen in Fig. 8a, the RWS anomaly shows a center of negative values near the west coast of Africa, in close correspondence

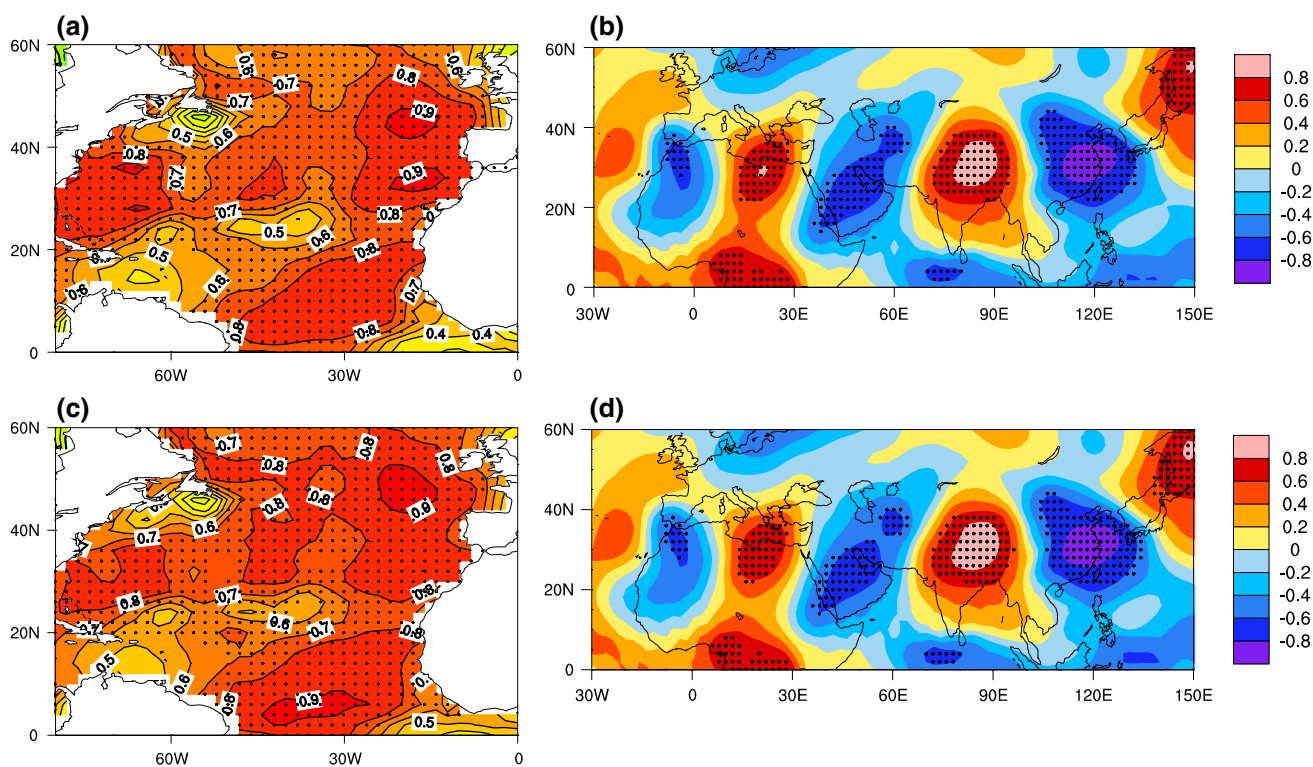


Fig. 7 Spatial patterns of the decadal-scale relation between the AAMT and AMV. **a** Correlation map between the cold season AAMT index and North Atlantic SST (0° – 60° N) at decadal timescales. **b** As in **a**, but for the AMV index and V300 anomalies over (0 – 60° N, 30° W– 150° E). **c**, **d** Spatial patterns of the leading MCA mode for the cold season **c** North Atlantic SST and **d** V300 anomalies over

(0 – 60° N, 30° W– 150° E) at decadal timescales, shown as correlation maps of the respective heterogeneous SST and V300 fields with the MCA leading normalized expansion coefficients. In **a**–**d**, *dots* indicate the correlations significant at the 95 % confidence level, and in the *dotted* areas, the N^{eff} varies spatially between 4 and 11, 5 and 14, 4 and 12 and 6 and 14, respectively

to the upper-level divergence. The locations of the anomaly centers of upper-level divergence and RWS are also in concert with the SST anomaly pattern of AMV, which generally has a reverse “C” or horseshoe shape with relatively large amplitudes off the west coast of Africa and Europe (Alexander et al. 2014).

Figure S4 of the Supplementary Material further shows the correlation maps of SST, precipitation and upper-level divergence fields associated with the AMV index at decadal timescales. Although the AMV is a basin-wide pattern, it shows highest positive correlations of SST along the Northwest coast of the North Africa. Following the SST pattern, the correlation maps of precipitation and upper-level divergence are both characterized by strongest positive correlations over the Northwest coast of the North Africa. The close relationships of the regional atmospheric conditions can be attributable to the underlying SST forcing: the AMV SST warming over the region may induce anomalous ascending motions that favors increased precipitation and upper-level divergence anomalies. Therefore, these results are useful to understand how the AMV induces the anomalous RWS over the Northwest coast of the North Africa. In

addition, the eastward wave activity flux of AAMT (shown in Fig. 5) emanates from the northwest coast of Africa, corresponding to a wave activity flux divergence (source of wave activity) there. Thus, the location of the RWS anomaly associated with the AMV is also consistent with the wave activity flux pattern of AAMT, further suggesting the dynamical linkage between AMV and AAMT.

Previous studies have found that in winter, a zonal wave train originating from the Mediterranean is closely related to the NAO at intraseasonal to interannual timescales, because the NAO can generate a wave source over the Mediterranean that excites the wave train downstream (Branstator 2002; Watanabe 2004). In this study, we focus on the connection of the AMV in the North Atlantic Ocean with the AAMT wave train pattern, which is prominent at multidecadal timescales and emanates from the northwest coast of Africa. We also calculated the correlation between the AAMT index and decadal NAO index for the cold season. The NAO index used here is defined as the PC time series associated with the EOF1 of cold season sea level pressure (from 20CRv2 dataset) over the North Atlantic region. The simultaneous correlation is very low

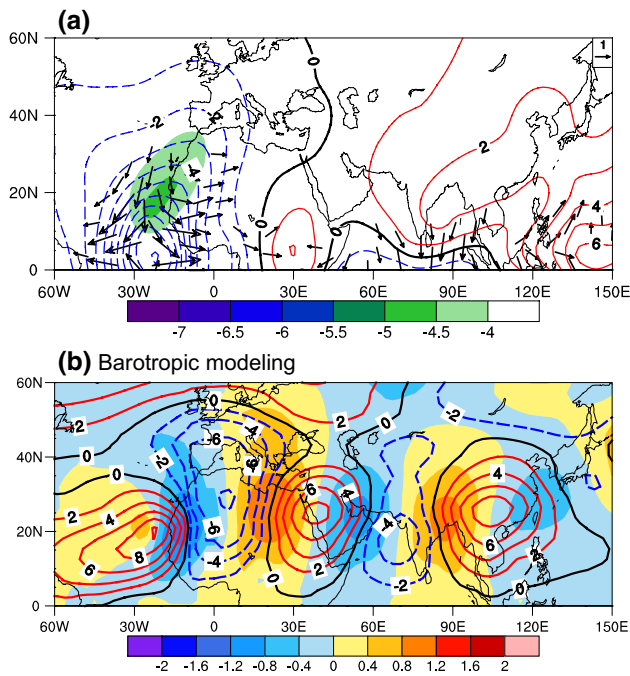


Fig. 8 **a** 300-hPa RWS (shading; 10^{-11} s^{-2} , only absolute values larger than $4 \times 10^{-11} \text{ s}^{-2}$ are plotted), velocity potential (contours, interval is $10^5 \text{ m}^2 \text{ s}^{-1}$) and divergent wind (vectors; m s^{-1}) anomalies associated with the AMV during the cold season, shown as regressions onto the normalized AMV index at decadal timescales. **b** Linear barotropic model responses of 300-hPa geopotential height (contours, interval is 2 m) and meridional wind (shading, m s^{-1}) to the idealized vorticity forcing centered at 20°N, 20°W. The geopotential height was obtained by multiplying the streamfunction by the Coriolis parameter

and insignificant ($r = -0.15$), indicating that the NAO has little direct effect on the AAMT wave train at multidecadal timescales.

We carry out a linear barotropic modeling experiment to examine the steady Rossby wave response to the RWS anomaly shown in Fig. 8a. Here, the cold season climatology of the 300-hPa streamfunction serves as the basic flow. The barotropic model responses of V300 and geopotential height (Fig. 8b) strongly project onto the observed patterns of the AAMT. In particular, the simulated height forced by the RWS exhibits an eastward propagating wave train with alternate centers of ridges and troughs, downstream of the forcing. The zonal scale of the simulated wave response is at wavenumbers 5–6, in agreement with the AAMT. Moreover, the response pattern shows three positive centers of height anomaly over Northwest Africa, the Arabian Peninsula and East Asia, similar to the observed height anomalies of AAMT. The placement and pattern of the simulated V300 anomalies are also consistent with the AAMT. Thus, the numerical experiment suggests that the AMV-related RWS anomaly can indeed excite the AAMT wave train. Furthermore, the simulated wave train is embedded in the

waveguide along the Asian jet stream, indicating a guiding effect of the Asian jet stream during the cold season.

We further perform Rossby wave ray tracing analysis to investigate the role of the Asian jet stream. Figure 9 shows the rays of stationary waves with zonal wavenumber 5 and 6 from several initial points located within the North Atlantic RWS region, which are in accordance with the AMV-related RWS anomaly. Zonal wavenumbers 5 and 6 are chosen to correspond to the zonal scale of AAMT. The cold season climatology of the 300-hPa zonal wind is used as the background field for the wave ray tracing. The rays for zonal wavenumber 5 and 6 both show a clear eastward propagation from the RWS region, in good agreement with the pathway of the AAMT wave train. This further suggests that the RWS near the northwest coast of Africa can induce pronounced eastward Rossby wave propagation, consistent with the barotropic modeling result. Moreover, the eastward wave trajectories are mainly trapped on the Asian jet stream, suggesting that the jet stream channels wave activity all the way to East Asia. To better show the waveguide created by the Asian jet stream, we calculated the total stationary wavenumber K_s based on the cold season basic zonal flow. As shown in Fig. 10, large total wavenumbers ($K_s \geq 5$) are observed along the Asian jet stream extending from the subtropical North Atlantic to East Asia and hence the cold season Asian jet stream acts as a Rossby waveguide (Hoskins and Ambrizzi 1993; Watanabe 2004). This indicates that stationary waves of higher wavenumber, like the AAMT, tend to be trapped on the jet stream. Therefore, the above analysis highlights the role of the Asian jet stream in guiding the AAMT wave train from the North Atlantic to East Asia.

3.3 AAMT as an atmospheric bridge conveying the AMV influence onto NA–EA LSAT

Previous studies have suggested that the NH mean LSAT shows pronounced multidecadal variations in the observational record (Jones et al. 2012; Wang et al. 2015). The NA–EA region covers a large portion of the NH land masses and thus an investigation of the LSAT multidecadal variability over NA–EA could be beneficial for deepening our understanding of the multidecadal fluctuations in the NH mean LSAT. The analysis above suggests that the AAMT is the dominant mode of multidecadal variability of the cold season upper-level circulation over the NA–EA region. As displayed in Fig. 11a, the LSAT over the NA–EA region is strongly related to the AAMT over multidecadal timescales. In particular, the LSAT field shows three significant centers of LSAT warming over Northwest Africa, the Arabian Peninsula and East Asia associated with the positive AAMT phase, and the locations of the warming centers are in good accordance with the geopotential height pattern of

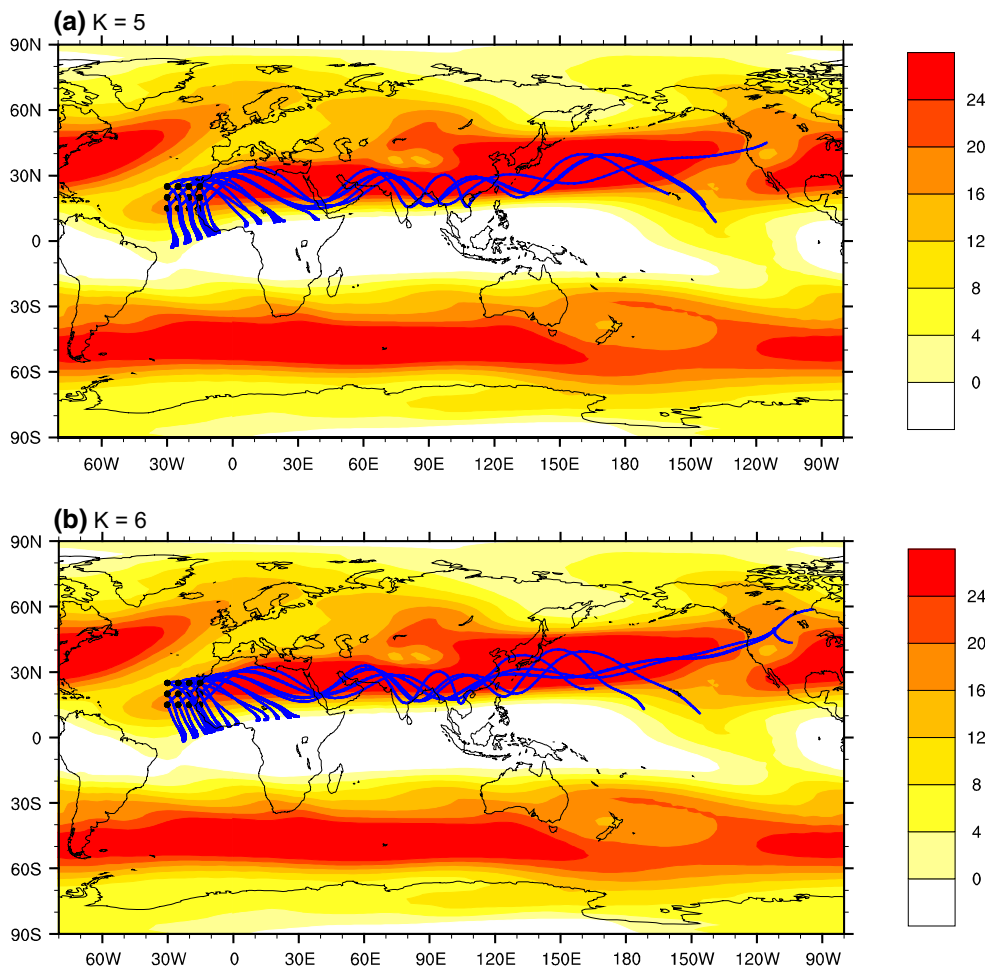
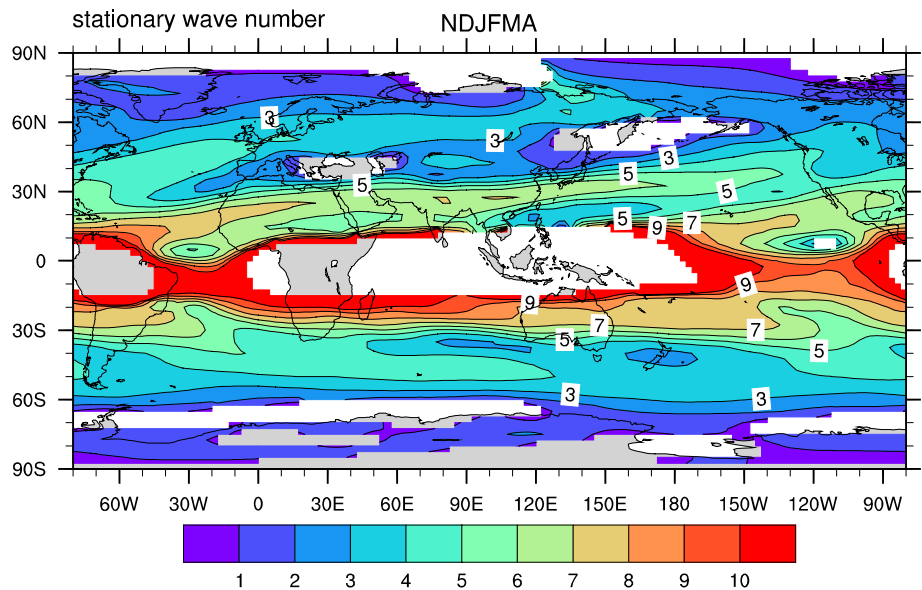


Fig. 9 Stationary Rossby wave trajectories (*blue curves*) with zonal wavenumber **a** $k = 5$ and **b** $k = 6$. The Rossby waves start from the west coast of Africa according to the RWS analyses shown in Fig. 8, and are forced by the background state of the cold season climatol-

ogy. The climatological mean 300-hPa zonal wind for the cold season (*color shading*; $m\ s^{-1}$) serves as the background field for the Rossby wave trains. The trajectories are computed by Rossby wave ray tracing analysis, following Li et al. (2015)

Fig. 10 Climatological Rossby stationary wavenumber ($\sqrt{(\beta - \bar{U}_{yy})/\bar{U}}$, where \bar{U} and β are mean zonal wind and meridional gradient of planetary vorticity, respectively, and $-\bar{U}_{yy}$ is the approximated meridional gradient of relative vorticity). The stationary Rossby wavenumber calculation is based on the long-term climatological zonal wind at 300 hPa for the cold season



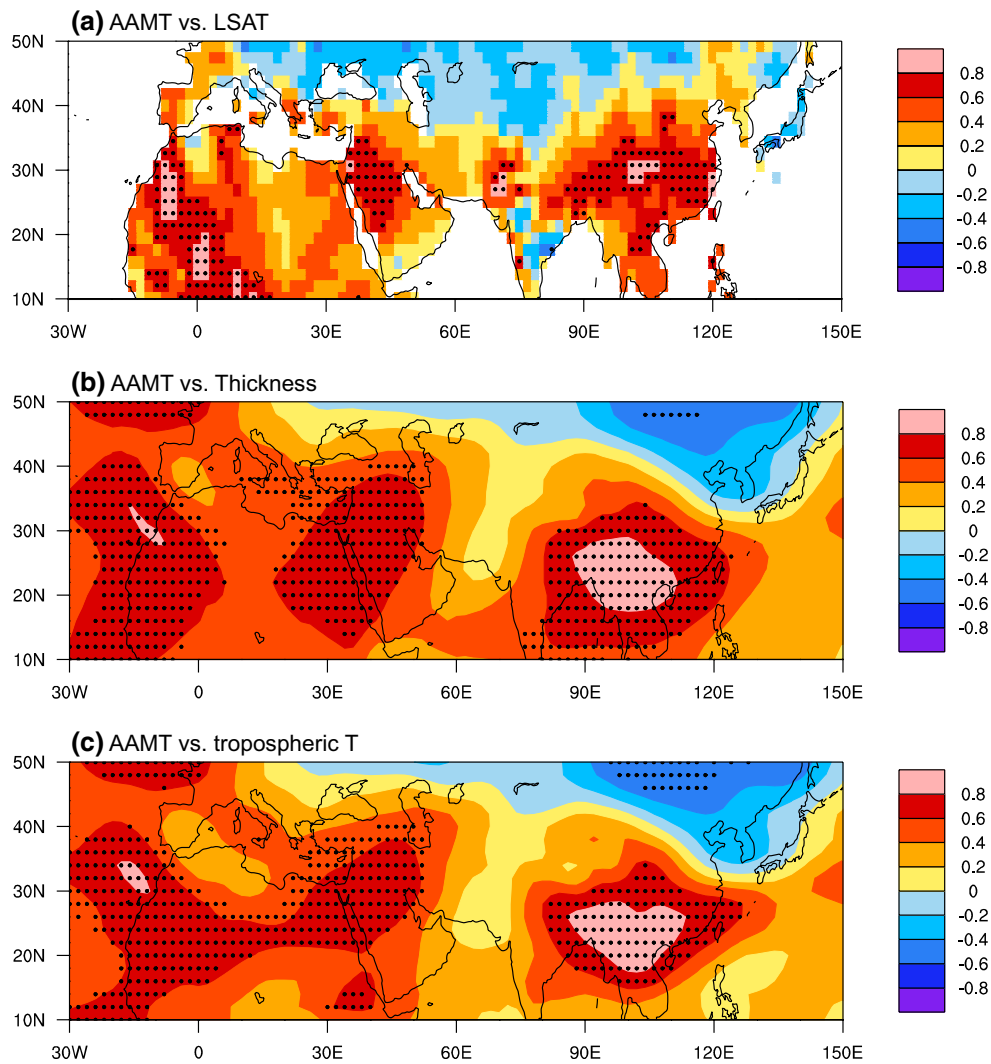


Fig. 11 Correlation maps of cold season **a** LSAT, **b** 300–1000 hPa thickness and **c** 300–1000 hPa tropospheric mean air temperature with the AAMT index at decadal timescales. Dots in **a–c** indicate the

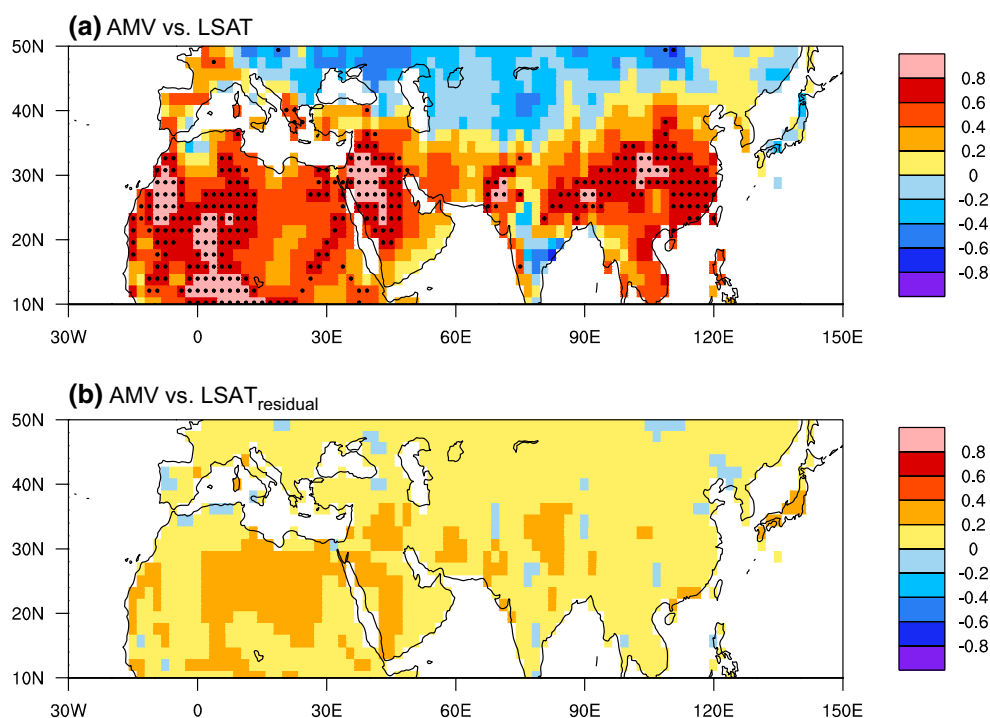
correlations significant at the 95 % confidence level, and in the *dotted* areas, the N^{eff} varies spatially between 5 and 15, 6 and 14 and 6 and 14, respectively

the AAMT (Fig. 5). Previous studies have suggested that the upper-level atmospheric circulation over mid-latitude land masses is relatively insensitive to warming/cooling of the local LSAT (Tang et al. 2013; Sun et al. 2016). Moreover, Wallace et al. (1996) have pointed out that upper-level atmospheric circulation could exert a profound influence on LSAT and tropospheric air temperature by adiabatic expansion and compression. To investigate this influence, we provide an analysis of the atmospheric thickness from the surface to the upper level (300–1000 hPa) associated with the AAMT (Fig. 11b). The thickness pattern is characterized by three centers of expansion of the air (increased air column thickness) across the NA–EA region. This is in good agreement with the three centers of higher-than-normal upper-level geopotential height in the AAMT wave train (vertical structure of AAMT in Fig. 4). The rising/falling of

upper-level geopotential height is usually associated with increased/decreased air column thickness (adiabatic expansion/compression of air) over the extratropical land regions during the cold season (Wallace et al. 1996). This indicates that the AAMT could indeed lead to adiabatic expansion/compression of the air over the NA–EA region.

According to the hypsometric equation, which relates the thickness to the tropospheric air temperature, the thickness between two pressure levels is directly proportional to the mean temperature of the air between those levels. As expected, the tropospheric mean air temperature averaged from the surface to the upper level (300–1000 hPa) shows a similar zonal wave train pattern (Fig. 11c) to the air column thickness (Fig. 11b) and upper-level geopotential height (Fig. 5). The tropospheric temperature pattern is also consistent with the LSAT pattern associated with the AAMT,

Fig. 12 **a** Correlation map between the cold season LSAT and AMV index at decadal timescales. *Dots* indicate the correlations significant at the 95 % confidence level, and in the *dotted* areas, the N^{eff} varies spatially between 5 and 14. **b** As in **a**, but for the LSAT data after removing the effect of AAMT (by subtracting the regression onto the AAMT index from the LSAT data)



showing three significant warming centers over Northwest Africa, the Arabian Peninsula and East Asia, respectively. In fact, the decadal LSAT over these land areas is highly positively correlated with the tropospheric temperature aloft in each grid cell (not shown here), indicating that there is strong vertical coupling of the air temperature from the troposphere to the land surface. This is consistent with the findings in (Wallace et al. 1996) that the cold season LSAT is closely coupled to the tropospheric temperature aloft at decadal timescales over the extratropical region, and this vertical coupling is helpful to understand the AAMT–LSAT connection. Therefore, in association with the AAMT, the atmospheric conditions (i.e., atmospheric thickness from the surface to the upper level, tropospheric air temperature and LSAT) exhibit consistent zonal wave train patterns across the NA–EA region. We also found that the LSAT pattern shown in Fig. 11a is one of the leading EOFs (the second EOF mode) of the LSAT decadal variation over the NA–EA region (Fig. S5 of the Supplementary Material). The corresponding PC time series is also highly correlated with the AAMT index ($r = 0.90$, significant at the 95 % confidence level), furthering supporting that the decadal variability of the NA–EA LSAT is closely tied to the upper-level AAMT wave train.

The connection between AAMT and the NA–EA LSAT is important for understanding the mechanism of the downstream climate influence of the AMV. Figure 12a displays the correlation map of the cold season NA–EA LSAT with the AMV index, for 11-year running mean data. The correlation map shows three centers of significant positive

correlation (maxima exceeding 0.8) located over Northwest Africa, the Arabian Peninsula and Central China. The strong link between cold season LSAT over China and AMV is consistent with previous findings that the warm AMV phase is associated with warmer-than-normal winter LSAT over most of China (Li and Bates 2007; Wang et al. 2009). Previous studies have suggested that Pacific Decadal Oscillation (i.e., PDO) can influence East Asian winter LSAT variations (Wu et al. 2011; Wu and Zhang 2015). We found that for the 1901–2012 period, the decadal cold season LSAT has statistically significant correlations with the PDO only over Northeast China (not shown here), and this is different from the LSAT pattern associated with the AMV. The connections of cold season LSAT over Northwest Africa and the Arabian Peninsula with the AMV have not been clearly addressed in the literature. Previous studies have suggested that during summer, Northwest Africa shows significant cold LSAT anomalies in association with the warm AMV phase (Sutton and Hodson 2005). This indicates a seasonal dependence of the AMV influence on the LSAT multidecadal variability over Northwest Africa. More importantly, the above analysis suggests a coordinated change in LSAT over Northwest Africa, the Arabian Peninsula and Central China in response to the AMV. The correlation map between AMV and LSAT also closely resembles the pattern of LSAT influenced by the AAMT (shown in Fig. 11a). This suggests that the AAMT acts as an atmospheric bridge conveying the AMV influence onto the downstream multidecadal climate variability. To highlight the atmospheric bridge of the AAMT, we repeated the

correlation analysis shown in Fig. 12a, but for the LSAT data after removing the effect of the AAMT (by subtracting the regression onto the AAMT index from the LSAT data). As shown in Fig. 12b, the correlations become substantially lower, and no statistically significant correlation is found over the NA–EA region. Thus, the mechanism for the downstream influence of AMV on the cold season LSAT is clear; that is, the change in the LSAT across the NA–EA region is influenced by the upper-level AAMT wave train, which is remotely forced by the AMV through Rossby wave dynamics.

4 Summary and Discussion

Using 112 years of Twentieth Century Reanalysis data, we identified a multidecadal teleconnection pattern by EOF analysis of the multidecadal variations of cold season (November to April) upper-level meridional wind over North Africa and Eurasia (NA–EA). This teleconnection pattern is characterized by an eastward propagating Rossby wave train with a zonal wavenumber of 5–6 between 20° and 40°N, extending from the northwest coast of Africa to East Asia, and thus is referred to as the Africa–Asia multidecadal teleconnection pattern (AAMT). One-point correlation maps for the centers of action in the AAMT further suggest that the teleconnectivity of AAMT is strong. Although the AAMT is most prominent in the upper-level meridional wind, it is also seen in the geopotential height throughout the troposphere. The AAMT shapes the spatial structure of multidecadal change in atmospheric circulation over the NA–EA region; in particular, the AAMT pattern and associated fields show similar structures to the multidecadal change in circulation occurring around the early 1960s. Thus, our analysis supports the notion that the AAMT is a distinct pattern of the atmospheric circulation multidecadal variability over the subtropical NA–EA region.

A better understanding of the mechanism for the remote influence of AMV is important not only for extending our knowledge of the AMV climate impact, but also for interpreting the multidecadal variability in both proxy data and observational records. A strong in-phase relationship is observed between the AMV and AAMT and the associated mechanism is mainly Rossby wave dynamics. North Atlantic SST anomalies of the AMV can induce upper-level divergence/convergence anomalies, which lead to an anomalous Rossby wave source (RWS) centered near the northwest coast of Africa. Results from barotropic modeling and Rossby wave ray tracing suggest that the RWS associated with the AMV can excite the AAMT wave train and that the Asian jet stream plays a crucial role in guiding the wave train to East Asia. The results also explain why the

AAMT appears to be trapped on the Asian jet stream. Thus, our analysis provides a dynamical insight into the AMV–AAMT connection. Multidecadal variability in the NA–EA land surface air temperature (LSAT) is strongly related to the AMV, and in particular coordinated changes in LSAT over Northwest Africa, the Arabian Peninsula, and Central China are found to be connected to the AMV. The coordinated changes in the NA–EA surface and tropospheric air temperatures may result from the adiabatic expansion/compression of air associated with the AAMT wave train. Thus, the AAMT further acts as an atmospheric bridge conveying the influence of AMV onto the downstream multidecadal climate variability.

In this study, we have focused on the cold season AAMT and its relation to the AMV. Sun et al. (2015b) have found that during the warm season, the AMV can force a Rossby wave train with a zonal wavenumber of 3–4 across northern Eurasia. This warm season wave train differs from the AAMT in spatial scale and propagation pathway, indicating a seasonally varying influence of the AMV on the downstream climate. The major feature of the AMV SST anomaly pattern, basin-wide warming/cooling in the North Atlantic, is essentially the same throughout the year due to the slow ocean processes (Sutton and Hodson 2003, 2007). Even though the SST forcing pattern is seasonally invariant, a seasonal dependence of the forced Rossby wave response is indeed expected. The propagation of Rossby waves is highly sensitive to the background flow (Hoskins and Karoly 1981). During the cold season, the westerly winds are much stronger than in the warm season and the Asian jet stream extends far westward to the North Atlantic, providing favorable conditions for Rossby wave propagation along the Asian jet stream. This mechanism may partly account for the seasonal dependence of the Rossby wave response. Further investigations on this issue are necessary but beyond the scope of this study. In addition, because the AMV shows a significant periodicity of around 50–70 years (Sun et al. 2015a; Schlesinger and Ramankutty 1994; Delworth and Mann 2000), the dynamical relationship of the AMV with the AAMT and cold season climate over the NA–EA region may have implications for decadal prediction and interpretation of proxy data records; further analysis is also needed to investigate the AAMT–AMV connection within state-of-the-art coupled ocean–atmosphere general circulation models.

Acknowledgments The authors wish to thank the anonymous reviewers for their constructive comments that significantly improved the quality of this paper. This work was jointly supported by the National Key Research and Development Plan (2016YFA0601801), the National Science Foundation of China (41290255 and 41405128), and the National Programme on Global Change and Air-Sea Interaction (GASI-IPOVAI-06 and GASI-IPOVAI-03).

Reference

- Alexander MA, Halimeda Kilbourne K, Nye JA (2014) Climate variability during warm and cold phases of the Atlantic Multidecadal Oscillation (AMO) 1871–2008. *J Marine Syst* 133:14–26
- Booth BB, Dunstone NJ, Halloran PR, Andrews T, Bellouin N (2012) Aerosols implicated as a prime driver of twentieth-century North Atlantic climate variability. *Nature* 484(7393):228–232. doi:[10.1038/nature10946](https://doi.org/10.1038/nature10946)
- Branstator G (2002) Circumglobal teleconnections, the jet stream waveguide, and the North Atlantic Oscillation. *J Clim* 15(14):1893–1910
- Bretherton CS, Smith C, Wallace JM (1992) An intercomparison of methods for finding coupled patterns in climate data. *J Clim* 5(6):541–560
- Compo GP, Whitaker JS, Sardeshmukh PD et al (2011) The twentieth century reanalysis project. *Q J R Meteorol Soc* 137:1–28
- Corti S, Weisheimer A, Palmer TN, Doblas-Reyes FJ, Magnusson L (2012) Reliability of decadal predictions. *Geophys Res Lett.* doi:[10.1029/2012gl053354](https://doi.org/10.1029/2012gl053354)
- DelSole T, Tippett MK, Shukla J (2011) A significant component of unforced multidecadal variability in the recent acceleration of global warming. *J Clim* 24(3):909–926. doi:[10.1175/2010jcli3659.1](https://doi.org/10.1175/2010jcli3659.1)
- Delworth TL, Mann ME (2000) Observed and simulated multidecadal variability in the Northern Hemisphere. *Clim Dyn* 16(9):661–676
- Delworth TL, Zhang R, Mann ME (2007) Decadal to centennial variability of the Atlantic from observations and models. In: *Ocean circulation: mechanisms and impacts*. Geophysical monograph series 173. American Geophysical Union, Washington, DC, pp 131–148
- Ding QH, Wang B (2005) Circumglobal teleconnection in the Northern Hemisphere summer. *J Clim* 18(17):3483–3505
- Ding YH, Liu YJ, Liang SJ, Ma XQ, Zhang YX, Si D, Liang P, Song YF, Zhang J (2014) Interdecadal variability of the east asian winter monsoon and its possible links to global climate change. *J Meteorol Res* 28(5):693–713. doi:[10.1007/s13351-014-4046-y](https://doi.org/10.1007/s13351-014-4046-y)
- Enfield DB, Mestas-Nunez AM, Trimble PJ (2001) The Atlantic multidecadal oscillation and its relation to rainfall and river flows in the continental US. *Geophys Res Lett* 28(10):2077–2080
- Enomoto T, Hoskins BJ, Matsuda Y (2003) The formation mechanism of the Bonin high in August. *Q J R Meteorol Soc* 129(587):157–178. doi:[10.1256/gj.01.211](https://doi.org/10.1256/gj.01.211)
- Folland CK, Rayner NA, Brown SJ, Smith TM, Shen SSP, Parker DE, Macadam I, Jones PD, Jones RN, Nicholls N, Sexton DMH (2001) Global temperature change and its uncertainties since 1861. *Geophys Res Lett* 28(13):2621–2624. doi:[10.1029/2001gl012877](https://doi.org/10.1029/2001gl012877)
- Gastineau G, Frankignoul C (2011) Cold-season atmospheric response to the natural variability of the Atlantic meridional overturning circulation. *Clim Dyn* 39(1–2):37–57. doi:[10.1007/s00382-011-1109-y](https://doi.org/10.1007/s00382-011-1109-y)
- Gray ST (2004) A tree-ring based reconstruction of the Atlantic Multidecadal Oscillation since 1567 A.D. *Geophys Res Lett.* doi:[10.1029/2004gl019932](https://doi.org/10.1029/2004gl019932)
- Greatbatch RJ (2000) The North Atlantic Oscillation. *Stoch Environ Res Risk Assess* 14(4–5):213–242
- Hansen J, Ruedy R, Sato M, Lo K (2010) Global surface temperature change. *Rev Geophys.* doi:[10.1029/2010rg000345](https://doi.org/10.1029/2010rg000345)
- Harris I, Jones PD, Osborn TJ, Lister DH (2014) Updated high-resolution grids of monthly climatic observations—the CRU TS3.10 dataset. *Int J Climatol* 34(3):623–642. doi:[10.1002/joc.3711](https://doi.org/10.1002/joc.3711)
- Hodson DLR, Sutton RT, Cassou C, Keenlyside N, Okumura Y, Zhou TJ (2010) Climate impacts of recent multidecadal changes in Atlantic Ocean sea surface temperature: a multimodel comparison. *Clim Dyn* 34(7–8):1041–1058
- Hoskins BJ, Ambrizzi T (1993) Rossby-wave propagation on a realistic longitudinally varying flow. *J Atmos Sci* 50(12):1661–1671
- Hoskins BJ, Karoly DJ (1981) The steady linear response of a spherical atmosphere to thermal and orographic forcing. *J Atmos Sci* 38(6):1179–1196
- Hsu HH, Lin SH (1992) Global teleconnections in the 250-mb streamfunction field during the Northern-Hemisphere winter. *Mon Weather Rev* 120(7):1169–1190
- Jones PD, Lister DH, Osborn TJ, Harpham C, Salmon M, Morice CP (2012) Hemispheric and large-scale land-surface air temperature variations: an extensive revision and an update to 2010. *J Geophys Res.* doi:[10.1029/2011jd017139](https://doi.org/10.1029/2011jd017139)
- Knight JR, Allan RJ, Folland CK, Vellinga M, Mann ME (2005) A signature of persistent natural thermohaline circulation cycles in observed climate. *Geophys Res Lett.* doi:[10.1029/2005gl024233](https://doi.org/10.1029/2005gl024233)
- Kucharski F, Molteni F, Yoo JH (2006) SST forcing of decadal Indian Monsoon rainfall variability. *Geophys Res Lett.* doi:[10.1029/2005gl025371](https://doi.org/10.1029/2005gl025371)
- Kucharski F, Bracco A, Yoo JH, Tompkins AM, Feudale L, Ruti P, Dell’Aquila A (2009) A Gill-Matsuno-type mechanism explains the tropical Atlantic influence on African and Indian monsoon rainfall. *Q J R Meteorol Soc* 135(640):569–579. doi:[10.1002/qj.406](https://doi.org/10.1002/qj.406)
- Latif M, Keenlyside NS (2011) A perspective on decadal climate variability and predictability. *Deep Sea Res Part II* 58(17–18):1880–1894. doi:[10.1016/j.dsr2.2010.10.066](https://doi.org/10.1016/j.dsr2.2010.10.066)
- Latif M, Boning C, Willebrand J, Biastoch A, Dengg J, Keenlyside N, Schweckendiek U, Madec G (2006a) Is the thermohaline circulation changing? *J Clim* 19(18):4631–4637
- Latif M, Collins M, Pohlmann H, Keenlyside N (2006b) A review of predictability studies of Atlantic sector climate on decadal time scales. *J Clim* 19(23):5971–5987
- Li S, Bates GT (2007) Influence of the Atlantic multidecadal oscillation on the winter climate of East China. *Adv Atmos Sci* 24(1):126–135. doi:[10.1007/s00376-007-0126-6](https://doi.org/10.1007/s00376-007-0126-6)
- Li S, Perlwitz J, Quan X, Hoerling MP (2008) Modelling the influence of North Atlantic multidecadal warmth on the Indian summer rainfall. *Geophys Res Lett.* doi:[10.1029/2007gl032901](https://doi.org/10.1029/2007gl032901)
- Li JP, Sun C, Jin FF (2013) NAO implicated as a predictor of Northern Hemisphere mean temperature multidecadal variability. *Geophys Res Lett* 40(20):5497–5502
- Li YJ, Li JP, Jin FF, Zhao S (2015) Interhemispheric propagation of stationary rossby waves in a horizontally nonuniform background flow. *J Atmos Sci* 72(8):3233–3256. doi:[10.1175/Jas-D-14-0239.1](https://doi.org/10.1175/Jas-D-14-0239.1)
- Lu RY, Oh JH, Kim BJ (2002) A teleconnection pattern in upper-level meridional wind over the North African and Eurasian continent in summer. *Tellus A* 54(1):44–55
- Lu RY, Dong BW, Ding H (2006) Impact of the Atlantic multidecadal oscillation on the Asian summer monsoon. *Geophys Res Lett.* doi:[10.1029/2006GL027655](https://doi.org/10.1029/2006GL027655)
- Nigam S, Guan B, Ruiz-Barradas A (2011) Key role of the Atlantic multidecadal oscillation in 20th century drought and wet periods over the Great Plains. *Geophys Res Lett.* doi:[10.1029/2011gl048650](https://doi.org/10.1029/2011gl048650)
- North GR, Bell TL, Cahalan RF, Moeng FJ (1982) Sampling errors in the estimation of empirical orthogonal functions. *Mon Weather Rev* 110(7):699–706
- Omrani NE, Bader J, Keenlyside NS, Manzini E (2015) Troposphere–stratosphere response to large-scale North Atlantic Ocean variability in an atmosphere/ocean coupled model. *Clim Dyn.* doi:[10.1007/s00382-015-2654-6](https://doi.org/10.1007/s00382-015-2654-6)
- Plumb RA (1985) On the 3-dimensional propagation of stationary waves. *J Atmos Sci* 42(3):217–229

- Rayner NA, Parker DE, Horton EB, Folland CK, Alexander LV, Rowell DP (2003) Global analyses of sea surface temperature, sea ice, and night marine air temperature since the late nineteenth century. *J Geophys Res* 108:4407. doi:[10.1029/2002JD002670](https://doi.org/10.1029/2002JD002670)
- Schlesinger ME, Ramankutty N (1994) An oscillation in the global climate system of period 65–70 years. *Nature* 367(6465):723–726
- Smith TM, Reynolds RW, Peterson TC, Lawrimore J (2008) Improvements to NOAA's historical merged land-ocean surface temperature analysis (1880–2006). *J Clim* 21(10):2283–2296. doi:[10.1175/2007jcli2100.1](https://doi.org/10.1175/2007jcli2100.1)
- Sun C, Li JP, Jin FF, Ding RQ (2013) Sea surface temperature inter-hemispheric dipole and its relation to tropical precipitation. *Environ Res Lett*. doi:[10.1088/1748-9326/8/4/044006](https://doi.org/10.1088/1748-9326/8/4/044006)
- Sun C, Li JP, Jin FF, Xie F (2014) Contrasting meridional structures of stratospheric and tropospheric planetary wave variability in the Northern Hemisphere. *Tellus A*. doi:[10.3402/Tellusa.V66.25303](https://doi.org/10.3402/Tellusa.V66.25303)
- Sun C, Li JP, Jin FF (2015a) A delayed oscillator model for the quasi-periodic multidecadal variability of the NAO. *Clim Dyn* 45(7–8):2083–2099. doi:[10.1007/s00382-014-2459-z](https://doi.org/10.1007/s00382-014-2459-z)
- Sun C, Li JP, Zhao S (2015b) Remote influence of Atlantic multidecadal variability on Siberian warm season precipitation. *Sci Rep*. doi:[10.1038/srep16853](https://doi.org/10.1038/srep16853)
- Sun C, Li JP, Ding RQ (2016) Strengthening relationship between ENSO and western Russian summer surface temperature. *Geophys Res Lett* 43(2):843–851. doi:[10.1002/2015GL067503](https://doi.org/10.1002/2015GL067503)
- Sutton RT, Hodson DLR (2003) Influence of the ocean on North Atlantic climate variability 1871–1999. *J Clim* 16(20):3296–3313
- Sutton RT, Hodson DLR (2005) Atlantic Ocean forcing of North American and European summer climate. *Science* 309(5731):115–118. doi:[10.1126/science.1109496](https://doi.org/10.1126/science.1109496)
- Sutton RT, Hodson DLR (2007) Climate response to basin-scale warming and cooling of the North Atlantic Ocean. *J Clim* 20(5):891–907. doi:[10.1175/jcli4038.1](https://doi.org/10.1175/jcli4038.1)
- Tang QH, Zhang XJ, Yang XH, Francis JA (2013) Cold winter extremes in northern continents linked to Arctic sea ice loss. *Environ Res Lett*. doi:[10.1088/1748-9326/8/1/014036](https://doi.org/10.1088/1748-9326/8/1/014036)
- Teng H, Branstator G (2012) A zonal wavenumber 3 pattern of Northern Hemisphere Wintertime Planetary wave variability at high latitudes. *J Clim* 25(19):6756–6769. doi:[10.1175/jcli-d-11-00664.1](https://doi.org/10.1175/jcli-d-11-00664.1)
- Ting MF, Kushnir Y, Seager R, Li CH (2009) Forced and internal twentieth-century SST trends in the North Atlantic. *J Clim* 22(6):1469–1481. doi:[10.1175/2008jcli2561.1](https://doi.org/10.1175/2008jcli2561.1)
- Vellinga M, Wu PL (2004) Low-latitude freshwater influence on centennial variability of the Atlantic thermohaline circulation. *J Clim* 17(23):4498–4511. doi:[10.1175/3219.1](https://doi.org/10.1175/3219.1)
- Wallace JM, Zhang Y, Bajuk L (1996) Interpretation of interdecadal trends in Northern Hemisphere surface air temperature. *J Clim* 9(2):249–259
- Wang Y, Li S, Luo D (2009) Seasonal response of Asian monsoonal climate to the Atlantic multidecadal oscillation. *J Geophys Res*. doi:[10.1029/2008jd010929](https://doi.org/10.1029/2008jd010929)
- Wang ZM, Zhang XD, Guan ZY, Sun B, Yang X, Liu CY (2015) An atmospheric origin of the multi-decadal bipolar seesaw. *Sci Rep*. doi:[10.1038/Srep08909](https://doi.org/10.1038/Srep08909)
- Watanabe M (2004) Asian jet waveguide and a downstream extension of the North Atlantic Oscillation. *J Clim* 17(24):4674–4691
- Wu ZW, Zhang P (2015) Interdecadal variability of the mega-ENSO-NAO synchronization in winter. *Clim Dyn* 45(3–4):1117–1128
- Wu ZW, Li JP, Jiang ZH, He JH (2011) Predictable climate dynamics of abnormal East Asian winter monsoon: once-in-a-century snowstorms in 2007/2008 winter. *Clim Dyn* 37(7–8):1661–1669
- Wu ZW, Li JP, Jiang ZH, Ma TT (2012) Modulation of the Tibetan Plateau Snow cover on the ENSO teleconnections: from the East Asian summer monsoon perspective. *J Clim* 25(7):2481–2489. doi:[10.1175/Jcli-D-11-00135.1](https://doi.org/10.1175/Jcli-D-11-00135.1)
- Wu ZW, Zhang P, Chen H, Li Y (2015) Can the Tibetan Plateau snow cover influence the interannual variations of Eurasian heat wave frequency? *Clim Dyn*. doi:[10.1007/s00382-015-2775-y](https://doi.org/10.1007/s00382-015-2775-y)
- Zhang R, Delworth TL (2006) Impact of Atlantic multidecadal oscillations on India/Sahel rainfall and Atlantic hurricanes. *Geophys Res Lett*. doi:[10.1029/2006gl026267](https://doi.org/10.1029/2006gl026267)
- Zhang R, Delworth TL, Held IM (2007) Can the Atlantic Ocean drive the observed multidecadal variability in Northern Hemisphere mean temperature? *Geophys Res Lett*. doi:[10.1029/2006gl028683](https://doi.org/10.1029/2006gl028683)
- Zhou YF, Wu ZW (2016) Possible impacts of mega-El Niño/Southern oscillation and Atlantic multidecadal oscillation on Eurasian heat wave frequency variability. *Q J R Meteorol Soc*. doi:[10.1002/qj.2759](https://doi.org/10.1002/qj.2759)